REVIEW PAPER: NANO-STRUCTURED MATERIALS (PARTICLES, FIBERS, COLLOIDS, COMPOSITES, ETC.)

3DOM-NiFe$_2$O$_4$ as an effective catalyst for turning CO$_2$ and H$_2$O into fuel (CH$_4$)

Yanan Ren[1] · Dongmei Zheng[1] · Linyan Liu[1] · Qiangsheng Guo[2] · Na Sha[2] · Zhe Zhao[1,3]

Abstract
Three-dimensional ordered macroporous NiFe$_2$O$_4$ (3DOM-NFO) powder was synthesized through the direct templating method combined with the sol–gel combustion technique. Polymethyl methacrylate (PMMA) spheres with different sizes were used as the hard templates. In order to understand the effect of PMMA spheres mean size on the structure and catalytic activity of synthesized 3DOM-NFO, the detailed characterization of the material was carried out by XRD, SEM, BET, XPS, UV–VIS, and DRS techniques. Direct hydrogenation production of CH$_4$ from CO$_2$ and H$_2$O was used to evaluate the catalysis performance of 3DOM-NFOs. The production of CH$_4$ evolution can reach 1040.8 µmol/g at 350 °C and ambient pressure when 300 nm template was used. It was concluded that the specific surface area and moderate concentration of oxygen vacancies are the crucial factors affecting the catalysis properties. Reasonably high turnover number of 0.244 and high CH$_4$ conversion efficiency of 0.897% were obtained in this study. 3DOM-NFO can be a promising catalyst for hydrocarbon fuel production by directly using CO$_2$ and H$_2$O as the safe and cheap feedstocks.

Graphical Abstract
CH$_4$ evolution over time for different 3DOM-NFO catalysts at 350 °C.
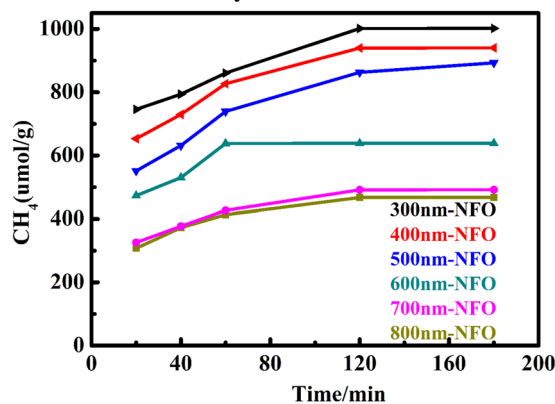
✉ Zhe Zhao
zhezhao@kth.se

Na Sha
shana@sit.edu.cn

[1] School of Materials Science and Engineering, Shanghai Institute of Technology, 201418 Shanghai, China

[2] School of Chemical and Environmental Engineering, Shanghai Insititue of Technology, 201418 Shanghai, China

[3] Department of Materials Science and Engineering, KTH Royal Institute of Technology, 10044 Stockholm, Sweden

Highlights

- 3DOM-NiFe$_2$O$_{4-\delta}$ can be synthesized successfully by using PMMA spheres as the hard template.
- A high CH$_4$ selectivity of >99% can be obtained for all 3DOM-NFO materials.
- For 50 mg catalyst, NFO-300 can promise a yield of 0.897% for the direct conversion of CO$_2$ and H$_2$O to CH$_4$ at 350 °C and ambient pressure.
- 3DOM-NFO catalyst developed in this study can be a very promising catalyst for hydrocarbon fuel production by directly using CO$_2$ and H$_2$O as the safe and cheap resources.

1 Introduction

Due to rapid industrialization, the over-consumption of fossil fuel reserves is accompanied with large anthropogenic CO$_2$ discharge, which is outpacing nature's CO$_2$ recycling capability and destroying the ecological balance, causing significant environmental harm, such as global warming and glaciers melting [1–3]. Meanwhile, the stock of oil and gas are not enough for a sustainable development in the future [4, 5]. The use of catalyst to chemically reduce CO$_2$ into hydrocarbon fuels, such as methanol or methane offers an efficient and feasible alternative to solve these problems [6]. It is a desirable goal to design and synthesize high-efficiency catalysts to convert CO$_2$ into fuels and chemicals [7].

Since Halmann [8] and Inoue [9] reported their pioneer work on the semiconductor photocatalysts for reduction of CO$_2$, many photocatalysts, such as TiO$_2$ [10–12], g-C$_3$N$_4$ [13], Bi$_2$WO$_6$ [14] SnNb$_2$O$_4$ [15] LaSrCoFeO$_{6-\delta}$ [16], ZnO@Cu–Zn–Al [17], have been developed for turning CO$_2$ into valuable hydrocarbon fuels, mostly in the form of CH$_4$. A photocatalyst is usually a semiconductor material which absorbs light, separates the photogenerated charges, transports them to the surface, and provides active sites for the catalytic reaction. However, the best CH$_4$ evolution performance is still less than 600 μmol/g. The reason is that breaking down C–O bonds needs higher energy. It was reported that an oxygen-deficient magnetite can break the chemical bond of CO$_2$ to form carbon at 300 °C [18], and the oxygen vacancies can enhance catalytic activity [19]. It is obvious that new catalysis process need to be explored. To consider the fact that most well-developed catalysis for organic synthesis is based on thermally driven process, then solar-driven thermochemical conversion can be one good option to be selected [20]. It will be a highly efficient way of using oxygen-deficient magnetite as catalyst for converting CO$_2$ hydrocarbon fuels on thermal reactions. Thanks to many well-designed solar irradiation collectors, solar-driven thermochemical reaction strategy can be easily implemented in reality. The key factor affecting the catalysis performance of catalyst is the concentration of oxygen vacancies [21, 22].

NiFe$_2$O$_4$, as a typical semiconductor material, was often used to carry out the redox reactions because the Fe ion exists as both bivalent and trivalent species [23]. It also shows an excellent chemical stability that has the advantage of low cost and simple preparation process. Based on these basic characteristics, we have demonstrated in our previous work that NiFe$_2$O$_4$ nanoparticles synthesized through solvothermal method can be a good catalyst to transform CO$_2$ and H$_2$O into CH$_4$ with almost 99.9% selectivity [24]. However, the CH$_4$ evolution rate is up to 357.6 μmol/g, which is still not high enough to make this material competitive for real application. A potential strategy for better catalysis performance is to increase surface area further.

This paper uses PMMA as the hard template, which was prepared by a convenient and efficient modified sol–gel combustion process to synthesize the 3DOM-NiFe$_2$O$_4$. The NiFe$_2$O$_4$ catalyst with higher specific surface area can be realized by such three-dimensional ordered macroporous structure [25, 26]. The unique ordered macroporous structure can display highly efficient ability for the adsorption of CO$_2$ and improve the transport and separation of electron–hole pairs [27]. Therefore, we report the preparation, characterization, and the catalytic properties of the three-dimensional ordered macroporous NiFe$_2$O$_4$ (3DOM-NFO) catalyst. The aim of this work was to investigate the effects of specific surface area and the concentration of oxygen vacancies on the catalytic reaction, crystal structure, catalytic performance, and thermal reaction mechanisms of the 3DOM-NFO for the CO$_2$ reduction.

2 Experimental

2.1 Synthesis of polymethyl methacrylate (PMMA) microspheres

PMMA spheres were synthesized by literature techniques [16, 28]. Potassium persulfate (6.0 mmol) and water (720 mL) were stirred at 300 rpm, heated at 90 °C, retained for 30 min, and degassed with flowing nitrogen in a separable three-neck 250 mL round-bottom flask. Methyl methacrylate (MMA, 748 mmol) was poured into the flask, and the

resulting suspension was stirred at 90 °C for 0.5, 1, 1.5, 2, 4, and 6 h, respectively. The PMMA colloidal crystal template was prepared by centrifugation (2500 rpm) of the colloidal suspension in a 50 mL centrifugation tube for 2 h. The different size template was obtained.

2.2 Preparation of 3DOM-NFO powders

The 3DOM-NFO powders were prepared by templating combined with sol–gel combustion method. A metal nitrate hydrate mixture (mole ratio: 0.015 M) and equal mole of citric acid $C_6H_8O_7$ hydrate mixture was dissolved with 8 mL of ethyleneglycol (EG) by stirring in a 100 mL beaker at room temperature for 2 h, and the produced EG solution was poured into a 25 mL volumetric flask. Methanol (8 mL) and EG were added in amounts necessary to achieve the desired concentration (the final concentration of methanol was 32 vol%). Then, the PMMA samples were soaked in the solution for 2 h. Excess solution was removed from the impregnated PMMA samples by vacuum filtration. After aging for 24 h in air it turned into a gel. A 0.5 g amount of the sample was mixed with 2.5 g of quartz sand (10–15 mesh) and calcined in a tubular furnace (inner diameter ca. 12 mm) in an air flow of 50 mL min. The temperature was raised at a rate of 1 °C/min to 600 °C and held for 5 h. the obtained powders were named 300 nm-NFO, 400 nm-NFO, 500 nm-NFO, 600 nm-NFO, 700 nm-NFO, and 800 nm-NFO.

2.3 Evaluation of catalytic activity

The thermocatalytic experiments were carried out in a gas-closed circulation system as shown in Fig. 1. 50 mg of the powder was uniformly placed at the bottom of a quartz reactor. The thermocatalytic activity evaluation was performed at 350 °C, which was kept through the heating jacket in out of the reactor and the temperature control device. In a period of insulation for 3 h, samples were taken every hour and quantitative analysis was performed on GS-Tek (Echromtek A90) equipment with a capillary column. The quantification of CH_4 yield was based on the external standard and the use of calibration curve.

3 Results and discussion

The PMMA spheres average particle size were characterized by Malvern size analyzer. Figure 2a shows that the PMMA spheres with different sizes were successfully synthesized. With the increase of PMMA sphere size, the size distribution becomes wider and harder to control. The XRD pattern of 3DOM-NFO particles templated by 300, 400, and 500 nm PMMA spheres can be indexed as the pure $NiFe_2O_4$ phase (PDF#01-086-2267), characteristic diffraction peaks at 2θ (°) = 30.3, 35.6, 37.3, 43.3, 53.8, 57.4, and 63.0 can be indexed as (2 0 0), (3 1 1), (2 2 2), (4 0 0), (4 2 2), (5 1 1), and (4 4 0) planes of face-centered cubic

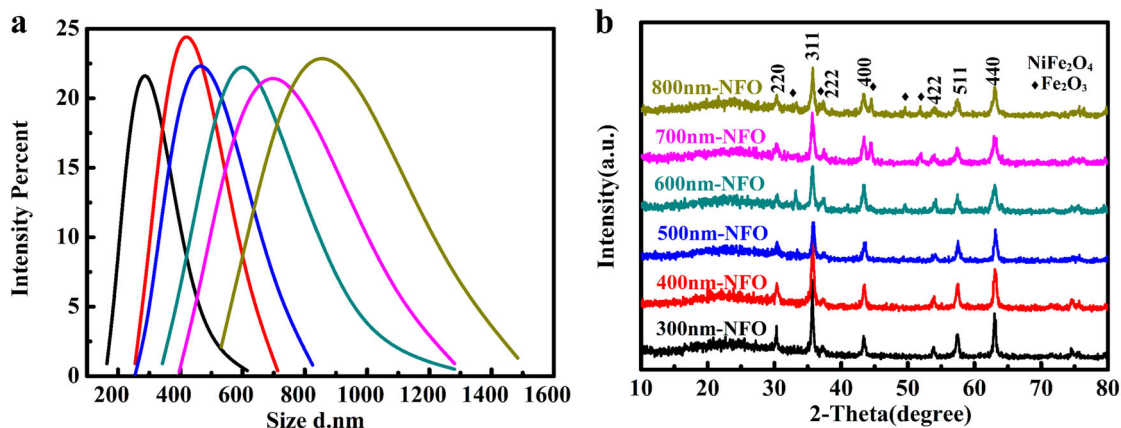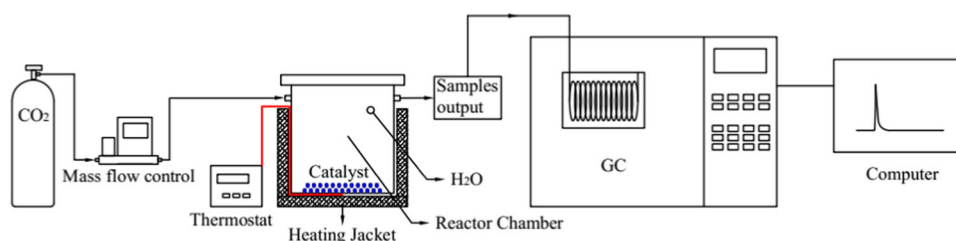Fig. 1 Schematic diagram for catalysis performance test

Fig. 2 a Average particle size distribution of PMMA spheres. b XRD pattern of 3DOM-NFO particles

Table 1 The XRD analysis and BET results of different 3DOM-NFO particles

Sample	S_{BET} (m²/g)	2θ (311) (°)	d_{311} (nm)	Unit cell a, b, c (nm)	Crystallite size (nm)
300 nm-NFO	153.3	35.683	0.2514	0.8344	27.2
400 nm-NFO	132.2	35.723	0.2511	0.8330	22.5
500 nm-NFO	123.0	35.799	0.2506	0.8316	20.5
600 nm-NFO	114.6	35.719	0.2512	0.8322	19.9
700 nm-NFO	99.6	35.681	0.2514	0.8332	19.7
800 nm-NFO	94.6	35.758	0.2509	0.8331	20.0

Fig. 3 SEM images of 3DOM-NFO synthesized by using different PMMA spheres of **a** 300 nm, **b** 600 nm, and **c** 800 nm. **d** PMMA spheres of 300 nm and **e** PMMA spheres of 600 nm
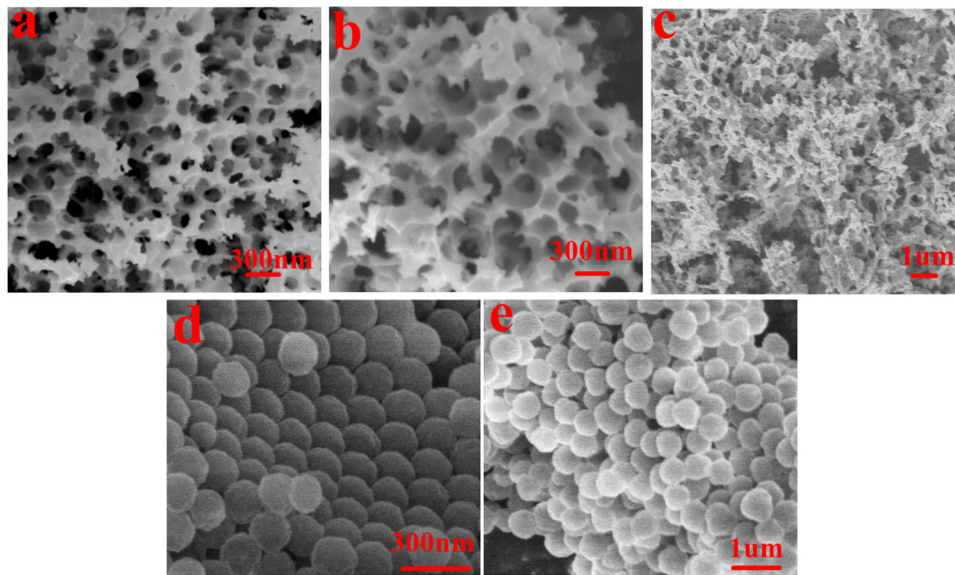
structure. For PMMA template spheres larger than 500 nm, impurity α-Fe₂O₃ phase (PDF #00-001-1053) can be clearly indexed in the XRD pattern (see Fig. 2b). Because the combustion of PMMA is an exothermic reaction, the local temperature is higher with the PMMA size increasing, this can be the key reason for the admixture formation. As seen from the data presented in Table 1, the crystallite size of 3DOM-NFO particles was determined using Debye–Scherrer's formula and found to be in the range of 19–28 nm. The BET-specific surface area decreases as the PMMA sphere size increase.

The SEM images of 3DOM-NFO catalysts and the PMMA colloidal crystal templates were clearly presented in Fig. 3. Except for the largest PMMA template size of 800 nm, the other 3DOM-NFO particles still reserved the original colloidal packing structure of spheres. The PMMA template ordered structure was replicated into NiFe₂O₄, we obtained the catalyst with macroporous structure successfully. The damage of the original packing structure in the 800 nm case can be linked with the higher local temperature during the combustion synthesis process. The local temperature linked with excess exothermal energy from relatively larger PMMA spheres seems to negatively affect both purity control and 3DOM structure reservation.
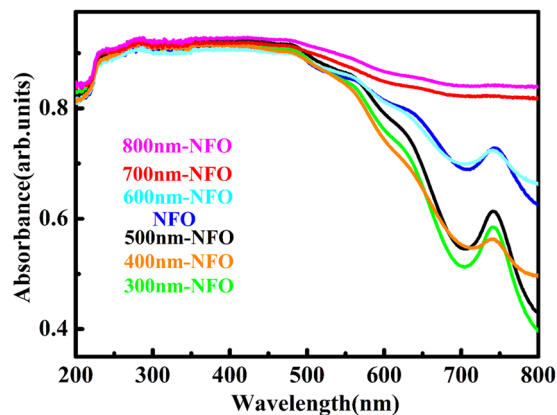
Fig. 4 UV–vis diffuse reflectance spectra of different 3DOM-NFO samples (indicated by different PMMA template sizes)

UV–vis diffuse reflectance spectra were measured and are shown in Fig. 4. For the samples of 300, 400, 500, 600 nm, the absorption peak around 740 nm is actually the characteristic absorption of NiFe₂O₄. This peak was totally smeared out in 700 and 800 nm samples due to the very much improved visible light absorption. The improved visible light absorption might be also linked with the high

local calcination temperature [29]. Higher temperature may introduce more oxygen vacancies in lattice and hence generate more intermediate energy levels in the band gap.

As shown in Table 1 and Fig. 5, the BET-specific surface areas of six 3DOM-NiFe$_2$O$_4$ samples changed with template sphere size, but the characteristic N$_2$-adsorption/desorption isotherms are rather similar, all presented with mesoporous pore channels. Specific surface area decreased from 153.3 to

Fig. 5 N$_2$ adsorption/desorption isotherm curves of 3DOM-NFOs

94.6 m^2/g when the template sphere size increased from 300 to 800 nm. Compared with the specific surface area of <25 m^2/g achieved with the solvothermally synthesized NFO nanoparticles [24], it is obvious that 3DOM structure is one efficient strategy to increase the surface area of catalyst. Larger surface area can lead to more reaction sites for CO$_2$ reduction.

X-ray photoelectron spectroscopy was used to investigate the chemical state and surface composition of the 3DOM-NFOs (see Fig. 6). Tables 2 and 3 list the key summary of such a XPS analysis. As shown in Fig. 6, the survey spectra (Fig. 6a) show peaks that are ascribed to Ni, Fe, O, and C. In Fig. 6b, The O 1s peak of 3DOM-NFOs (Fig. 6b) showed three Gaussian features at 530.2, 532.2, 533.5 eV, corresponding to the low, medium, and high binding energy peaks, respectively. which were attributed to lattice, surface, and adsorbed oxygen, respectively [30, 31]. In this case, it is possible to analyze the oxygen vacancies based on the previous reported methods [32, 33]. It has been reported that the surface oxygen component develops with the increase of oxygen vacancies [34], which can lead to the asymmetry of the main peak. Higher surface/lattice ratio indicate that more oxygen vacancies exist in the surface of
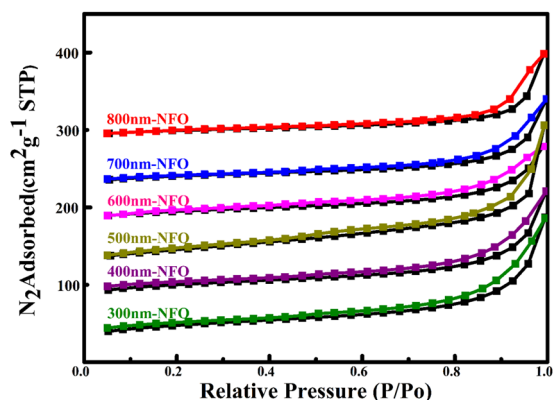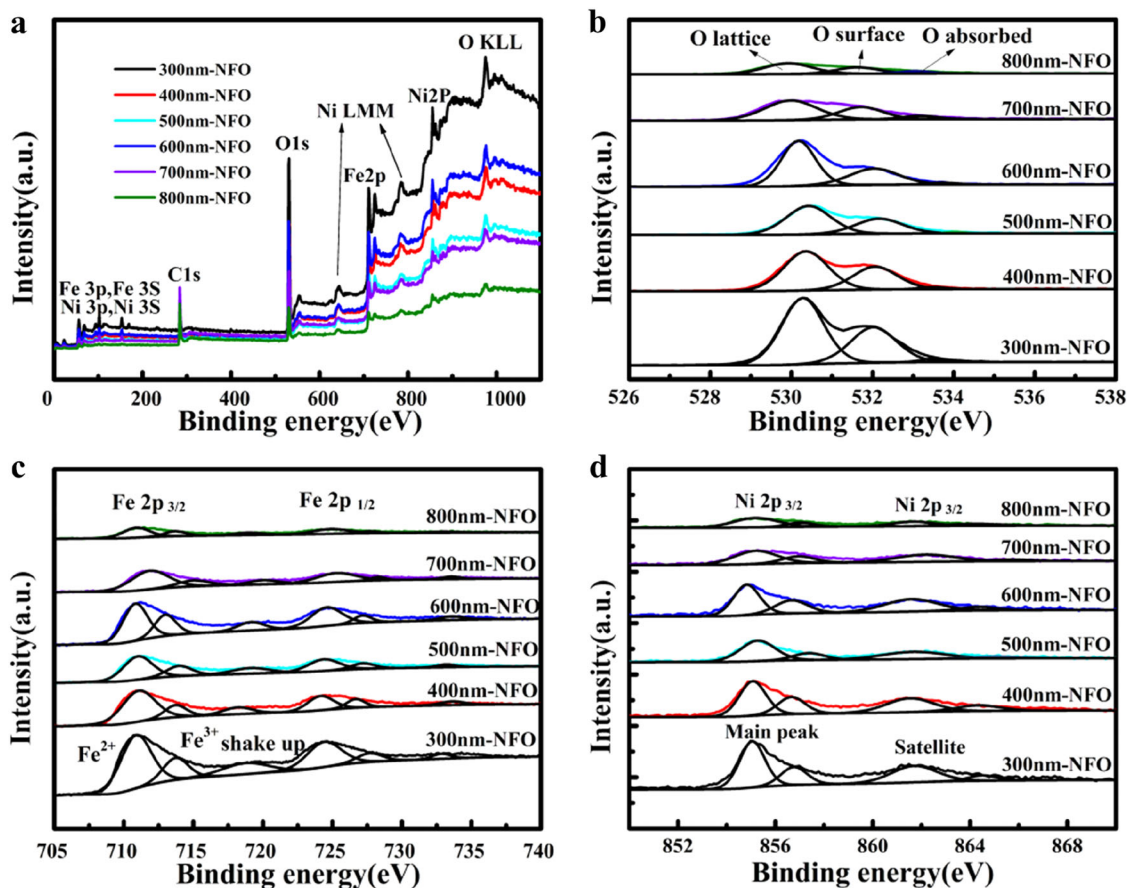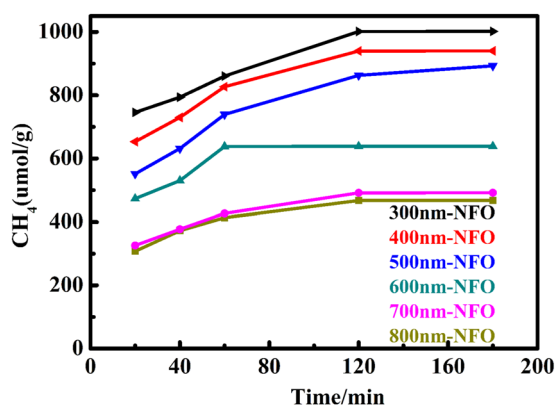

Fig. 6 The XPS spectra of **a** survey, **b** O 1s, **c** Fe 2p, and **d** Ni 2p of 3DOM-NFOs

Table 2 The relative concentrations of surface and lattice oxygen

O 1s (eV)	300 nm-NFO	400 nm-NFO	500 nm-NFO	600 nm-NFO	700 nm-NFO	800 nm-NFO
Lattice oxygen	61.66	61.78	63.49	64.28	60.73	59.69
Surface oxygen	36.25	36.19	35.21	33.5	32.36	31.78
Absorbed oxygen	2.09	2.03	1.30	2.22	6.91	8.53
Surface/lattice	0.59	0.59	0.55	0.52	0.53	0.53

Table 3 XPS-binding energies relative to the 3DOM-NFO. The relative concentrations of surface and lattice oxygen

Catalyst	Fe 2p (eV)		Ni 2p (eV)	
	Fe $2p_{3/2}$	Fe $2p_{1/2}$	Ni $2p_{3/2}$	Ni $2p_{1/2}$
300 nm-NFO	710.88 (74.58%)	724.41 (79.28%)	855.05 (70.91%)	861.70 (82.93%)
	713.72 (25.42%)	727.67 (20.72%)	856.76 (29.09%)	864.51 (17.07%)
400 nm-NFO	711.08 (79.39%)	724.16 (70.08%)	855.07 (66.10%)	861.52 (72.06%)
	713.72 (20.61%)	726.67 (29.92%)	856.66 (33.90%)	864.33 (27.94%)
500 nm-NFO	711.02 (72.21%)	724.38 (73.30%)	855.16 (72.67%)	861.84 (79.43%)
	713.97 (27.79%)	727.19 (26.70%)	856.82 (27.33%)	865.16 (20.57%)
600 nm-NFO	710.83 (66.70%)	724.58 (81.25%)	854.82 (65.32%)	861.58 (83.44%)
	713.98 (33.30%)	727.17 (18.75%)	856.66 (34.68%)	864.33 (16.56%)
700 nm-NFO	711.88 (78.56%)	725.29 (87.12%)	855.20 (71.64%)	862.10 (87.53%)
	714.99 (21.44%)	728.28 (12.88%)	856.94 (28.36%)	865.70 (12.47%)
800 nm-NFO	710.91 (70.80%)	724.88 (85.18%)	855.19 (78.12%)	861.67 (62.11%)
	713.69 (29.20%)	727.70 (14.82%)	857.02 (21.88%)	864.17 (37.89%)

Fig. 7 CH_4 evolution over time for different 3DOM-NFOs at 350 °C

listed in Table 3. The binding energy of Ni 2p were resolved by 855 and 857 for Ni $2p_{3/2}$ and 862 and 864 eV for Ni $2p_{1/2}$, respectively, which are similar to previously reported values [33]. Similarly, Fe 2p orbital were also resolved by 711 and 714 eV for Fe $2p_{3/2}$ and 724 and 727 eV for Fe $2p_{1/2}$ [16, 35]. However, a thorough analysis of the valence state in 3DOM-NFOs cannot lead to any consistent tendency when the template size was changed from 300 to 800 nm. It was so expected that it should be the specific surface area playing the key role for catalysis performance if finally a noticeable difference can be clarified in CO_2 hydrogeneration test.

In Fig. 7, the evolution of CH_4 with prolonged reaction time were presented for various 3DOM-NFOs. Among them, NFO-300 nm presented best performance with a cumulative yield of CH_4 up to 1040.8 μmol/g in 180 min. This value is four times of the best result we obtained in previous study and actually the reaction was finished in shorter time [25]. After the first two hours, the catalysis reaction almost reached the equilibrium state. It is also very interesting that we still get a very high selectivity (>99%, see Table 3) of CH_4. As we already discussed before, we can only identify specific area as the changing factor for different 3DOM-NFOs, It is more rational to ascribe the improvement of catalysis performance to the increased surface area in 300 nm-NFO. Furthermore, if we compare
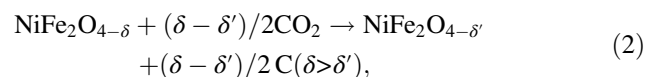
catalyst, which can be beneficial for CO_2 reduction process. However, shown by the data in Table 2, it is obvious that the calculated ratios of the surface oxygen to the lattice oxygen have not changed that much for different 3DOM-NFOs.

Besides the oxygen vacancy concentration, the valence state of transition metals is generally accepted to be another possible factor affecting the catalysis performance. From spectra presented in Fig. 6c, d, it is possible to deduce the ratio of Fe^{2+}/Fe^{3+} and Ni^{2+}/Ni^{3+} and all these results are

Table 4 Summary of yield and TON of CH_4 for different 3DOM-NFOs

Samples	Yield (%)[a] (CH_4)	TON[b] (CH_4)	Selectivity (%)
300 nm-NFO	0.897	0.244	>99
400 nm-NFO	0.810	0.220	>99
500 nm-NFO	0.769	0.209	>99
600 nm-NFO	0.550	0.150	>99
700 nm-NFO	0.423	0.115	>99
800 nm-NFO	0.403	0.110	>99

[a]Moles of product (CH_4) per mole of CO_2

[b]Turn over number = number of moles of product per mol of catalyst material

the evolution of CH_4 between various 3DOM-NFOs, the difference is roughly linearly linked with the change of surface area. Taking count of previous study with NFO, the improved CH_4 yield in this study can also be explained by the increased specific surface area. So the basic mechanism for CO_2 hydrogeneration with our NFOs should be the same as the one suggested by previous studies [25, 36, 37]. It was reported that $NiFe_2O_4$ with oxygen vacancies could transform H_2O into H under 350 °C (Eq. (1)) [36]. 3DOM-$NiFe_2O_{4-\delta}$ with more oxygen vacancies decomposes CO_2 into C around 350 °C (Eq. (2)) [37]. The generated carbon from the splitting of CO_2 will react with the hydrogen intermediate to form CH_4 (Eq. (3)) [24]. The high selectivity of >99% obtained in this study should be linked with the limited kinds of intermediate products possibly existed in our study. Very possibly, we have freshly formed C and H as the main intermediate molecules for CH_4 formation. But this is still a tentative proposal, which may need further detailed study.

$$NiFe_2O_{4-\delta} + (\delta - \delta')\,H_2O \rightarrow NiFe_2O_{4-\delta'} + 2(\delta - \delta')H, \tag{1}$$

$$NiFe_2O_{4-\delta} + (\delta - \delta')/2\,CO_2 \rightarrow NiFe_2O_{4-\delta'} + (\delta - \delta')/2\,C\,(\delta > \delta'), \tag{2}$$

$$C + 4H \rightarrow CH_4. \tag{3}$$
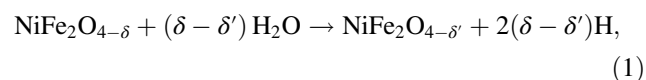
The yield of CH_4 can reach 0.897% (more details can be found in Table 4) and it can be anticipated to reach much better result if an industrial relevant condition. A turn over number (TON) of 0.244 was also recorded for 300 nm-NFO. To be more precise, there are still very limited catalyst which can realize efficient CO_2 hydrogeneration by using H_2O instead of H_2. 3DOM-NFO can be an efficient CO_2 hydrogeneration catalyst with low cost.

4 Conclusion

3DOM-$NiFe_2O_{4-\delta}$ can be synthesized successfully by using PMMA spheres as the hard template. Reasonably high specific surface area can be realized by this template strategy when combined with a sol–gel combustion method. The specific surface area is the key factor affecting the final catalysis performance for the reduction of CO_2 and H_2O to form hydrocarbon fuel CH_4. A high CH_4 selectivity of >99% can be obtained for all 3DOM-NFOS. For 50 mg 300 nm-NFO catalyst, the best production of CH_4 evolution can reach 1040.8 μmol/g for the direct conversion of CO_2 and H_2O to CH_4 at 350 °C and ambient pressure. A reasonably good TON of 0.244 was also reported for 300 nm-NFO. 3DOM-NFO catalyst developed in this study can be a very promising catalyst for hydrocarbon fuel production by directly using CO_2 and H_2O as the safe and cheap resources.

References

1. Raper SC, Braithwaite RJ (2006) Nature 439:311–313
2. Yang ZZ, He LN, Gao J et al. (2012) Energy Environ Sci 5:6602–6639
3. Olah GA, Prakash GK, Goeppert A (2011) J Am Chem Soc 133:12881–12898
4. Everest DA (1997) Energy & Environment, vol. 4. pp. 328–329.
5. Deffeyes KS (2006) Eco Econ 59:394–394
6. Habisreutinger SN, Schmidt-Mende L, Stolarczyk JK (2013) Angew Chem Int Ed 52:7372–7408
7. Neaţu Ş, Agulló M et al. (2014) Int J Mol Sci 15:5246–5262
8. Halmann M (1978) Nature 275:115–116
9. Inoue T, Fujishima A, Konishi S et al. (1979) Nature 277:637–638
10. Hashemizadeh I, Golovko VB, Choi J et al. (2018) Chem Eng J 347:64–73
11. Camarillo R, Tostón S, Martínez F et al. (2017) J Supercrit Fluid 123:18–27
12. Zhao H, Chen J, Rao G et al. (2017) Appl Surf Sci 404:49–56
13. Sun Z, Wang H, Wu Z et al. (2018) Catal Today 300:160–172
14. Xiao L, Lin R, Wang J et al. (2018) J Colloid Interface Sci 523:151–158
15. Zhu S, Liang S, Bi J et al. (2016) Green Chem 18:1355–1363
16. Ha MN, Lu G, Liu Z et al. (2016) J Mater Chem A 4:13155–13165
17. Guo Q, Zhang Q, Wang H et al. (2016) Catal Commun 77:118–122
18. Tamaura T (1990) Nature 346:255–256
19. Chen H, Yang M, Tao S et al. (2017) Appl Catal B 209:648–656
20. Meng X, Wang T, Liu L et al. (2015) Angew Chem Int Ed 53:11478–11482

21. Li D, Haneda H, Labhsetwar NK et al. (2005) Chem Phys Lett 40:579–584
22. Pan X, Yang MQ, Fu X et al. (2013) Nanoscale 5:3601–3614
23. Shin HC, Oh JH, Choi BC et al. (2004) Phys Status Solidi 1:3748–3753
24. Liu L, Cheng Y, Liu Z et al. (2016) RSC Adv 6:83814–83819
25. Imhof A, Pine DJ (2015) Nature 389:948–951
26. Holland BT, Blanford CF, Stein A (1998) Science 281:538–540
27. Wang T, Meng X, Liu G et al. (2015) J Mater Chem A 3:9491–9501
28. Sang ES, Kim K, Oh S et al. (2004) Macromol Res 12:240–245
29. Li X, Zhen X, Meng S et al. (2013) Environ Sci Technol 47:9911–9917
30. Zheng Y, Zheng L, Zhan Y et al. (2007) Inorg Chem 46:6980–6986
31. Naeem M, Hasanain SK, Kobayashi M et al. (2006) Nanotechnology 17:2675–2680
32. Puleo F, Liotta LF, La PV et al. (2014) Phys Chem Chem Phys 16:22677–22686
33. Yang Y, Tao Q, Srinivasan G et al. (2014) ECS J Solid State SC 3:P345–P352
34. Kim W, Choi M, Yong K (2015) Sens Actuators B Chem 209:989–996
35. Xu L, Ha MN, Guo Q et al. (2017) RSC Adv 7:45949–45959
36. Tamaura Y, Tahata M (1990) Nature 346:255–256
37. Tabata M, Nishida Y, Kodama T et al. (1993) J Mater Sci 28:971–974